Navier-Stokes Computations for Pointed, Spherical, and Flat Tipped Shell at Mach 3

Bernard J. Guidos* and Paul Weinacht*
U.S. Army Ballistic Research Laboratory, Aberdeen Proving Ground, Maryland 21005
and
David S. Dolling†
University of Texas at Austin, Austin, Texas 78758

A computational fluid dynamics study is described and results are shown for a tangent ogive-cylinder model with pointed, spherical, and flat nosetips at Mach number 2.95. The flow conditions simulate wind-tunnel tests conducted at the Princeton University Gas Dynamics Laboratory. The primary objective is to compare the computational and experimental results and assess the accuracy of the computational approach. Two thin-layer Navier-Stokes computational techniques are used in conjunction to compute the flowfields of interest. The first method computes the flow in the vicinity of the blunt nosetip and provides inflow conditions for the second method, which computes the flow over the remainder of the body, excluding the base region. Most of the comparisons of the nosetip flow structure, surface pressure distribution, and turbulent boundary-layer velocity profiles are within the measurement accuracy.

Nomenclature

a = speed of sound
d = reference diameter of model
p = pressure, normalized by $\rho_\infty a^2_\infty$
s = distance along body surface from nosetip vertex
u,v,w = Cartesian velocity components along x,y,z axes, respectively, normalized by a_∞
α = angle of attack
ϵ_e,ϵ_i = explicit and implicit numerical smoothing parameters, respectively
κ_ϵ = transition intermittency factor
μ = coefficient of molecular viscosity, normalized by freestream value
μ_{eff} = coefficient of effective viscosity, normalized by freestream value
μ_t = coefficient of effective turbulent viscosity, normalized by freestream value
ξ,η,ζ = transformed coordinates in the longitudinal, circumferential, and outward directions, respectively
ρ = density, normalized by freestream value
ϕ = roll angle (circumferential position on the body measured from windward side)

Subscript
∞ = freestream condition

Introduction

INTEREST in predicting nosetip bluntness effects on projectile aerodynamics at the U.S. Army Ballistic Research Laboratory (BRL) stems from the fact that almost all Army projectiles are blunt. Research has shown that nosetip bluntness can alter the Magnus characteristics of spinning shell.[1,2] The effects are manifested through detailed flow elements like the three-dimensional boundary layer and bow shock entropy

wake. With the computational power of the current generation of supercomputers, the flowfield can be simulated through large-scale Navier-Stokes computations.

The importance of validating blunt-body simulations with experimental measurements was demonstrated in Ref. 1. Predictions of the Magnus effect for models with pointed, spherical, and flat nosetips were compared to wind-tunnel measurements at Mach 3. The comparisons between computation and experiment for the sharp and spherical nosetip models were good, whereas the comparison for the flat nosetip model was poor. The findings were attributed to 1) the higher complexity of the flow over the flat nosetip compared to the spherical nosetip, and 2) the lack of sufficient size and speed of available computational resources to accurately model the flow over the flat nosetip.

Wind-tunnel tests were conducted to measure some of the effects of bluntness on the flow over a body of revolution, providing data for computational fluid dynamics (CFD) code validation. The tests were done at the Princeton University Gas Dynamics Laboratory for a tangent ogive-cylinder model with several different nosetips.[3-6] Surface-pressure measurements and boundary-layer pitot pressure surveys were made, and shadowgraphs were obtained at a freestream Mach number of 2.95.

More recently, a computational study was undertaken at BRL using thin-layer Navier-Stokes techniques to simulate the Princeton tests. Supercomputer resources not available for the study of Ref. 1 were used. The major objective was to compare the computational results with the wind-tunnel measurements and assess the accuracy of the CFD approach. The major results of the study are presented herein.

Wind-Tunnel Configurations and Flow Conditions

The computations simulate wind-tunnel tests conducted at the Princeton University Gas Dynamics Laboratory 20×20-cm Mach 3, high Reynolds number, blowdown tunnel. The models, instrumentation, techniques, and data acquisition and reduction are discussed in detail in the listed Refs 3–6. A brief description is given here to provide a background for the ensuing discussions.

The wind-tunnel model consists of a 3-caliber (cal) tangent ogive nose and a 6-cal cylindrical section, shown in Fig. 1. The reference diameter is that of the cylinder, 4.95 cm. For the wind-tunnel tests, three spherical nosetips and three flat

nosetips were manufactured to screw into the basic configuration in place of the pointed nosetip. The blunted nosetips were machined as truncations of the pointed nosetip, using three different bluntness ratios: 5, 12.5, and 25%. The bluntness ratio is defined here as the ratio of nosetip diameter to reference diameter. In the case of a spherical nosetip, the nosetip diameter is defined as twice the radial distance from the axis to the juncture of the sphere and ogive. For a flat nosetip, the nosetip diameter is defined as twice the radial distance from the axis to the juncture of the flat face and ogive.

In the tests, the model was supported at the base by an axial sting and held fixed relative to the freestream. Wall pressure distributions, pitot pressure surveys, and shadowgraphs were obtained. Longitudinal (streamwise) velocity profiles were generated from the pitot surveys, which were taken at three axial locations on the cylinder. The shadowgraphs provided a means for locating the bow shock, the boundary-layer transition zone, and, in the case of a flat nosetip, the imbedded recompression shock.

Conditions for the computations are taken as the average over numerous wind-tunnel runs. The Mach number is 2.95, with angles of attack of 0 and 2.9 deg. The nominal stagnation temperature is 260 K, the nominal Reynolds number is 3.14×10^6 based on model diameter, and the stagnation pressure is 6.89×10^5 N/m^2 (6.8 atm). The wall temperature is taken as adiabatic and the flow is assumed to be steady. Boundary-layer transition occurred in the experiment without the use of a tripping device and varied notably between the different nosetips. The computational simulation of transition is briefly discussed in a separate section.

This paper focuses on three nosetips in particular: the pointed nosetip (P), the spherical nosetip with 25% bluntness (R3), and the flat nosetip with 25% bluntness (F3); see Fig. 1. Nosetips R3 and F3 most clearly illustrate the effects of bluntness due to their comparatively large scales. Nosetip P provides the reference case for discerning these effects. In addition, the flowfield of nosetip F3 is clearly the most challenging case to model because of expected flow separation at the abrupt corner of the flat face.

Computational Approach

The computational methodology consists of two relatively well-known techniques applied in succession. An unsteady Navier-Stokes (UNS) technique is used to compute the flow in the vicinity of the blunt nosetips by numerically integrating the governing equations toward a steady-state solution. This provides initial conditions for a parabolized Navier-Stokes (PNS) technique, which computes the flow by integrating, or marching, the governing equations in the streamwise direction. The two approaches are briefly described. The reader is urged to consult Refs. 7-18 for complete details of the numerical approaches.
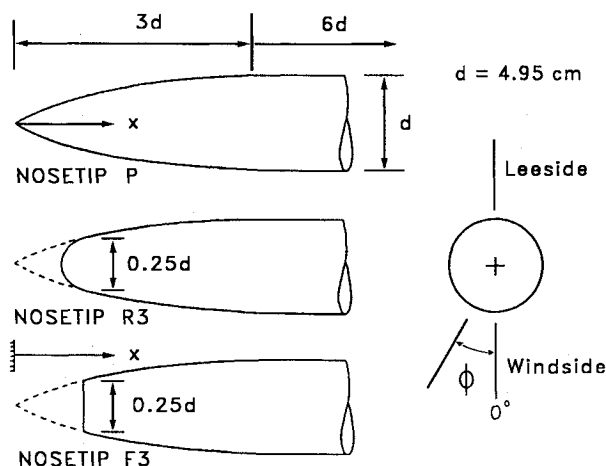

Fig. 1   Wind-tunnel model and nosetip configurations.

Thin-Layer Unsteady Navier-Stokes

The flow over the blunted nosetips was accomplished using the thin-layer UNS approach first reported by Pulliam and Steger.[7] This technique integrates the transformed, time-dependent, thin-layer, Reynolds-averaged, Navier-Stokes equations in strong conservation law form. The solution is advanced toward a steady state by numerically integrating through time using the approximately factored, implicit, delta form, finite difference algorithm of Beam and Warming.[8] Second-order central differencing is used in the three coordinate directions. For the spherical tip case at nonzero incidence, a directionally hybrid implicit/explicit algorithm was applied to eliminate implicit sweeps in the η and ξ directions in favor of more efficient explicit sweeps.[9]

The outer boundary, which consists of the bow shock, is shock fitted using an explicit procedure.[10] At the body surface, the no-slip velocity boundary condition is enforced and the pressure is updated explicitly from the normal momentum equation evaluated at the wall. The downstream (outflow) boundary employs a linear (constant outflow gradient) extrapolation along outflow grid lines. For the cases at nonzero incidence, bilateral symmetry conditions are imposed along the pitch plane. For the cases at zero incidence (axisymmetric flow), only one circumferential grid plane is used. The flowfield initialization procedure is described in Ref. 11.

The blunt-body solutions were generated using second-order-implicit and fourth-order-explicit smoothing terms, which are controlled by the parameters ϵ_i and ϵ_e respectively.[12] In the early stages of the computation, values of ϵ_i and ϵ_e were set at 0.3 and 0.1, respectively; these parameters were reduced, as the solution progressed, to the final values of 0.03 and 0.01, respectively.

Thin-Layer Parabolized Navier-Stokes

Computational modeling of the flow over the ogive and cylinder (and the pointed nosetip) was accomplished using the thin-layer PNS technique first reported by Schiff and Steger.[13] This technique spatially integrates the transformed, steady, thin-layer, Reynolds-averaged, Navier-Stokes equations in strong conservation law form. The solution is advanced downstream by numerically integrating in the streamwise direction using the approximately factored, implicit, delta form, finite difference algorithm of Beam and Warming.[8] Second-order central differencing is used in the circumferential and radial directions, and first-order one-sided differencing is used in the marching direction. Fourth-order-explicit smoothing is added to suppress high-frequency oscillations in the solution.

The outer boundary, which consists of the bow shock, is shock fitted using an implicit procedure.[14] At the body surface, the no-slip condition is enforced and the pressure is obtained from the subsonic sublayer approximation; that is, the pressure across the subsonic portion of the viscous layer is held constant. Bilateral symmetry conditions are imposed along the pitch plane. Initial conditions for the pointed nosetip configuration are generated using the PNS method in step-back mode.[14-16] The step-back procedure assumes conical flow conditions near the tip of the projectile and iteratively refines the solution to satisfy this assumption.

Code Coupling

The PNS procedure requires initial conditions for downstream marching. Initial conditions for marching consist of two adjacent ξ grid planes where the vector of dependent variables is known. For the blunt nosetip cases, the converged UNS solutions provide initial marching conditions. Each nosetip solution was nonconservatively interpolated onto a PNS grid at two adjacent axial stations. The circumferential grid distribution was retained exactly, and the dependent flow variables were linearly interpolated in the radial direction.

The location of initial conditions for the PNS computations was selected far enough downstream to avoid large streamwise gradients and, in the case of the F3 nosetip, flow separation

around the corner of the flat face. The initial data location was also selected far enough upstream from the UNS outflow boundary to avoid inaccuracies associated with the constant gradient outflow boundary condition. Trial and error in the early stages of the study revealed anomalies in the PNS solutions in either extreme. The PNS solutions that used blunt-body initial conditions for marching required no more explicit numerical smoothing than the PNS solutions that utilized the PNS conical step-back procedure.

Numerical Grids

Figures 2 and 3 show the computational grids for nosetips R3 and F3, respectively, on a constant circumferential plane. The computational grids were generated algebraically. For nosetip R3, a grid with dimensions 50×30 (that is, longitudinal $\times$ near normal) was used; for nosetip F3, a grid with dimensions 119×60 was used. As usual for viscous flow computations, grid points were clustered near the body to ensure resolution of the boundary layer. For the axisymmetric flow cases, a single circumferential plane was used. For the nonzero angle-of-attack cases, where bilateral symmetry exists, 21 grid planes were distributed circumferentially from $\phi = -10$ to 190 deg at 10-deg increments.

The F3 geometry was arrived at during the computation by truncating a small portion of the (initially) spherical nosetip, regenerating the grid, and allowing the solution to relax (about 500 time steps) several times during the solution procedure. This approach inherently required more computer time to obtain a converged solution, but was necessitated by the need to avoid numerical instabilities in the UNS solution.

The PNS computations were performed using cylindrical grids. In the radial direction, 45 grid points were used with exponential clustering near the body. For the nonzero angle-of-attack cases, grid planes were distributed circumferentially from $\phi = 0$ to 180 deg at 10-deg increments. For axisymmetric solutions, three circumferential planes were used at $\phi = 0$, 90, and 180 deg in order to employ a tested cylindrical coordinate formulation of the PNS equations.[14,16] The grid density in the marching direction varied from 300 to 500 marching steps over a length of approximately 8 cal.

Computer Resources

The blunt-nosetip computations were performed on Cray X-MP/48 and Cray 2 computers located at BRL. The computing times, memory usage, and approximate number of iterations for nosetips R3 and F3 are shown in Table 1. For nosetip F3, computational efficiency was compromised considerably in favor of obtaining a stable, accurate benchmark solution. The computational times shown in Table 1 are not intended to represent the CPU requirements of this computational approach in general.

The PNS computing times are given here for solutions that were marched a distance of 8 cal downstream. For the axisymmetric cases, the CPU time was about 30 s on a Cray X-MP. For the nonaxisymmetric cases, the CPU time was about 3 min on a Cray X-MP.

Boundary-Layer Transition

Boundary-layer transition occurred in the experiment without the use of a tripping device. In all cases, the flow appeared to be laminar near the nosetip. Transition can be seen in the shadowgraphs to occur on the ogive, but to vary as a
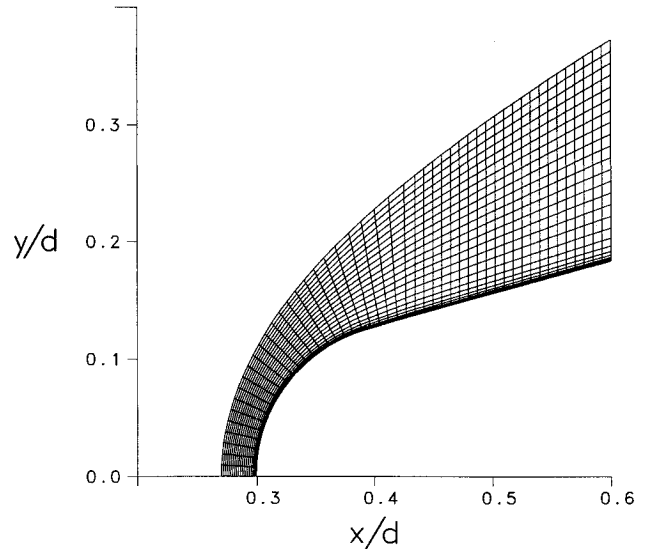

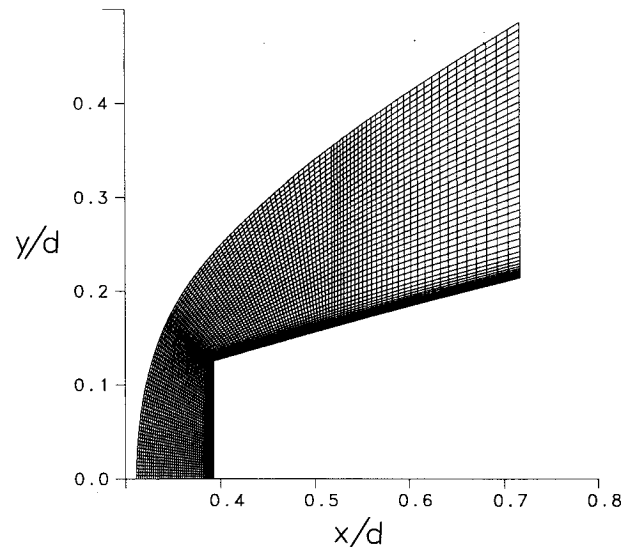Fig. 2   Computational grid for nosetip R3, $\alpha = 0$ deg.

Fig. 3   Computational grid for nosetip F3, $\alpha = 0$ deg.

function of nosetip geometry, angle of attack, and roll angle. As discussed in Ref. 6, the shadowgraphs provide additional insight into the phenomenon of transition for these tests. For purposes of computational validation, however, the presence of natural transition contributes uncertainties into the computational modeling of the flow. To establish consistency in the comparisons between computation and experiment, transition was prescribed a priori in all of the PNS computations to begin near the initial data plane and extend downstream approximately 1 cal. This simple approach of simulating transition is described as follows.

Following the shadowgraphs, all of the nosetip computations were performed using laminar flow conditions. In the PNS code, the effective viscosity μ_{eff}, usually defined as

$$\mu_{eff} = \mu + \mu_t \qquad (1)$$

Table 1   Computer resources

Tip	α, deg.	Mesh size, long. $\times$ norm. $\times$ circ	Computer	Memory, Mwords	CPU time	Number of iterations
R3	0	$50 \times 30 \times 1$	Cray X-MP/48	0.15	10 min	2,500
R3	2.9	$50 \times 30 \times 21$	Cray X-MP/48	0.55	3 h	3,000
F3	0	$119 \times 60 \times 1$	Cray 2	0.30	7.0 h	18,000
F3	2.9	$119 \times 60 \times 21$	Cray 2	2.50	40 h	5,000

was redefined as

$$\mu_{eff} = \mu + \kappa_\epsilon \mu_t \qquad (2)$$

where μ is the laminar (molecular) viscosity and μ_t the turbulent viscosity obtained from the Baldwin-Lomax turbulence model.[17] The transition intermittency factor κ_t is defined to be 0.0 for laminar flow and 1.0 for turbulent flow. Using distributions of intermittency based on the discussions in Ref. 18, κ_t was specified to vary continuously from 0.0 to 1.0 as a function of x along the ogive portion of the model. The sensitivity of the numerical results was investigated by varying the location and length of the transition region in the PNS code. The effect on the computed surface pressure was found to be negligible. However, the effect on the computed velocity profiles, especially at nonzero angle of attack, was sometimes as large as the effect due to bluntness itself. For this reason, the a priori specification of transition intermittency is considered important for ensuring that unbiased comparisons are made between computation and experiment.
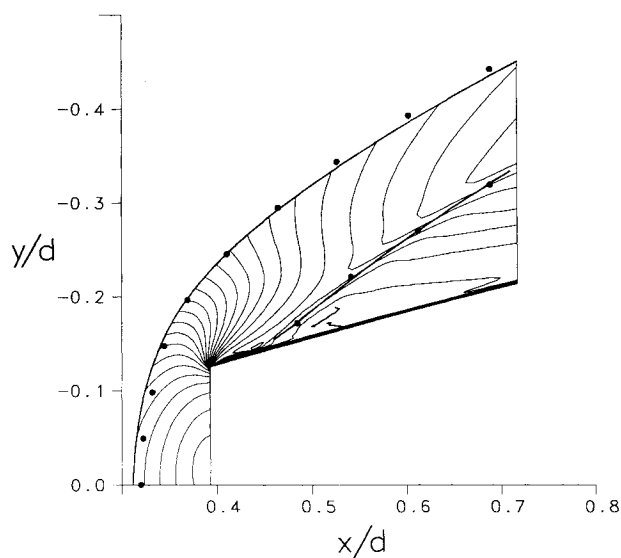
Fig. 4   Computed shocks and Mach contours (0.1–2.4 at 0.1 increments) and comparison with measured shocks, tip F3, $\alpha = 2.9$ deg, wind side.
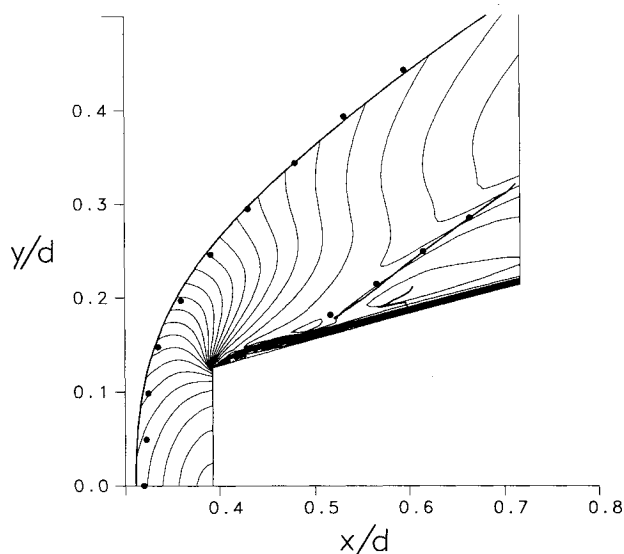

Fig. 5   Computed shocks and Mach contours (0.1–2.4 at 0.1 increments) and comparison with measured shocks, tip F3, $\alpha = 2.9$ deg, lee side.
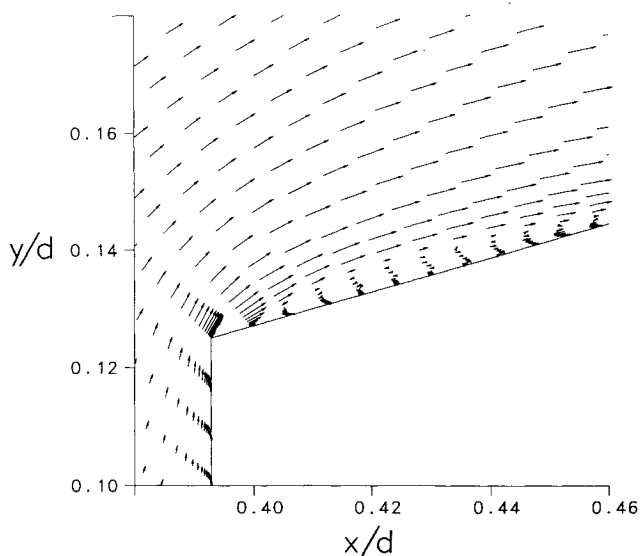

Fig. 6   Computed velocity vectors showing flow separation, tip F3, $\alpha = 0$ deg.

Results

Nosetip Flow Structure

The locations of the bow and recompression shocks of the various nosetips were determined using transparencies of the shadowgraphs. The uncertainty in the measured distance between any two points is approximately ± 0.002 cal. The uncertainty in the absolute radial location of the measured points is approximately ± 0.002 cal. The uncertainty in the absolute axial location of the measured points is approximately ± 0.0025 cal for nosetip R3 and ± 0.006 cal for nosetip F3. Details of the procedure that was used to determine the shock locations as well as measurement uncertainties are given in Ref. 19.

In Figs. 4 and 5, the computed Mach contours and shock patterns are shown for nosetip F3, $\alpha = 2.9$ deg. For comparison, the measured shock patterns are plotted as points. The strong expansion at the corner is visible in the Mach contours, but the recompression shock is less obvious due to its weakness and obliqueness. The computed imbedded shocks are instead visualized in the plot as thickened solid lines. These lines represent surfaces where the velocity component in the direction of the pressure gradient is equal to the local sound speed, and the Mach number in that direction is decreasing.[20] This particular shock pattern visualization algorithm also yields several extraneous, disconnected patches near the body.

The comparison of the computed and measured shock patterns is approximately within the accuracy of the measurement in each case. The trends with respect to incidence are well predicted along the pitch plane, with the bow shock moving closer to the body on the wind side and farther from the body on the lee side. The recompression shock is located farther upstream on the wind side than on the lee side. In Fig. 4, the slight bend in the recompression shock is apparent in both computation and experiment.

Whether flow separation occurs around the shoulder of the flat nosetip is difficult, if not impossible, to determine from the shadowgraphs. Figure 6 shows a close-up view of the computed velocity vectors for nosetip F3, $\alpha = 0$ deg. The computation shows that the flow separates downstream of the corner and reattaches approximately 0.1 cal downstream, illustrating the need for high grid resolution near the corner to adequately resolve the separation region. This was a computational aspect that was not achieved in the study of Ref. 1, where separation was not captured in the numerical solution of flow over a flat nosetip and the Magnus force was not well predicted. Additionally, since the flow is assumed to be laminar at the nosetip, turbulence modeling is not a factor in the computation of the separated flow region.
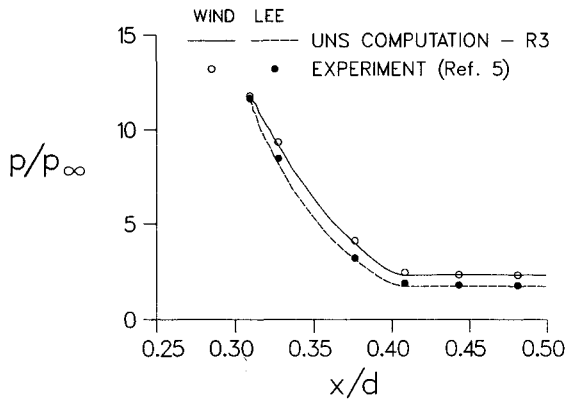
Fig. 7 Surface pressure comparison, tip R3, $\alpha = 2.9$ deg.
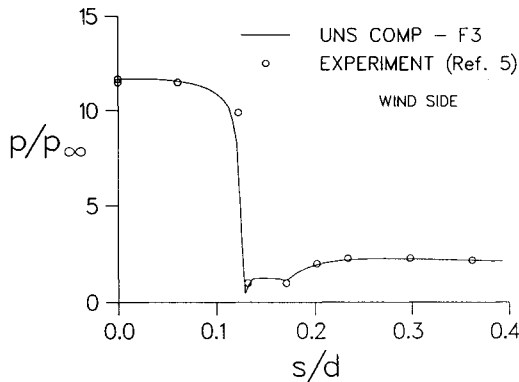

Fig. 8 Surface pressure comparison, tip F3, $\alpha = 2.9$ deg, wind side.

Surface Pressure

The accuracy of the surface pressure measurements is reported in Ref. 5 to be typically $\pm 1.0\%$ of the freestream static pressure. Larger variations in the data, due to changing stagnation conditions over the duration of the experiments, are indicated by the actual data. The measured stagnation point pressure varies by about $\pm 3\%$. Farther downstream, where different transducers were used, the largest variation is as large as $\pm 5\%$.

Figure 7 shows the comparison of the computed and measured surface pressure for nosetip R3, $\alpha = 2.9$ deg, wind and lee sides. The agreement between computation and experiment is within the experimental accuracy. The flow does not overexpand. Some minor wavering of the computed pressure—a slowly damping numerical oscillation—is shown near the nosetip vertex.

Figures 8 and 9 show the comparison of the computed and measured surface pressure for nosetip F3, $\alpha = 2.9$ deg, wind and lee sides. Near the stagnation point, the pressure agrees to within the experimental accuracy. The third pressure tap, located on the flat face of the nosetip, shows that the locally subsonic flow is already expanding before it reaches the corner. Whereas the computation shows its maximum disagreement with experiment at the third tap, the severe expansion appears to be qualitatively captured in the numerical solution. A closer examination of the grid and the Mach contours reveals that much of this expansion is captured near the body surface between two adjacent grid points. The tail end of the computed expansion shows a slight overshoot before recovering to a pressure level more comparable to that of the first tap downstream of the corner. Downstream of the corner, the flow overexpands and recompresses similarly in both the computation and the experiment. The computed pressures in the overexpanded region compare with the fifth pressure tap to within the measurement accuracy on the wind side. On the lee side, the computed pressure at the fifth tap is slightly lower

than the measured pressure. In each case, the computed surface pressure recovery level agrees with the experiment to within the measurement accuracy.

The pressure distribution and flow structure at the nosetip are important indicators of the localized effects of bluntness. Farther downstream, as reported in Refs. 4-6, the surface pressure shows a variation of only $\pm 1.5\%$ between the different nosetips. The velocity profiles, which are a more sensitive downstream indicator of bluntness, must be utilized for further computational validation.

Longitudinal Velocity Profiles

Figures 10 and 11 show the velocity profile comparisons for nosetips P and R3, $\alpha = 2.9$ deg. Throughout most of the boundary layer, the absolute agreement between computation and experiment is within 5%. The exception is at the second station on the lee side, where the agreement is within only about 8-9%. At each station, however, the comparisons
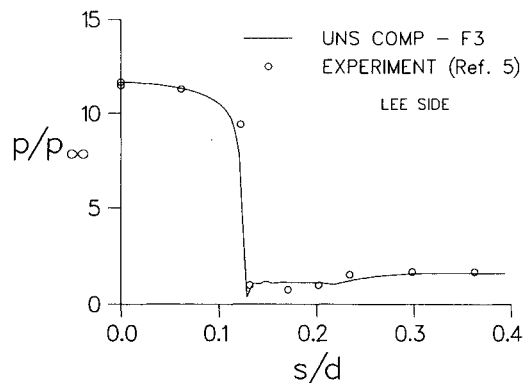

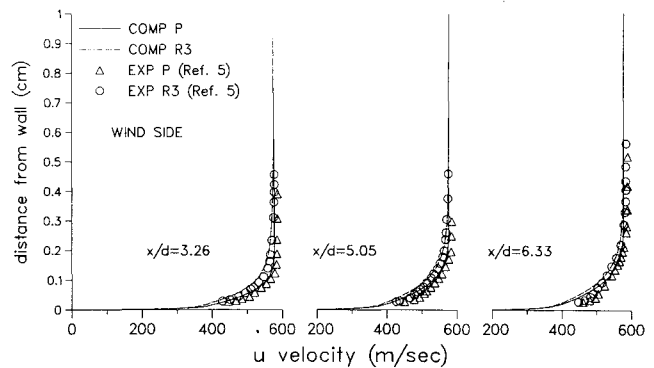Fig. 9 Surface pressure comparison, tip F3, $\alpha = 2.9$ deg, lee side.

Fig. 10 Velocity profile comparisons, tips P and R3, $\alpha = 2.9$ deg, wind side.
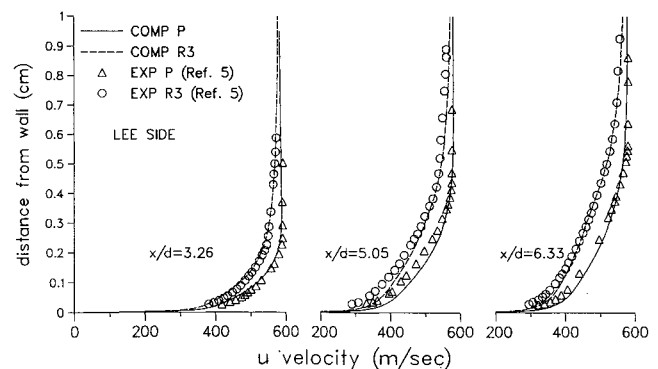

Fig. 11 Velocity profile comparisons, tips P and R3, $\alpha = 2.9$ deg, lee side.
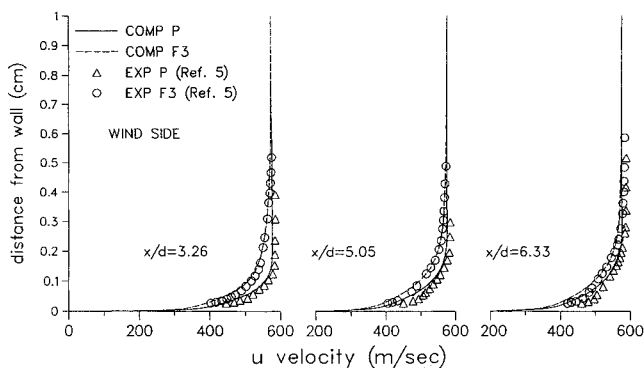
Fig. 12 Velocity profile comparisons, tips P and F3, $\alpha = 2.9$ deg, wind side.
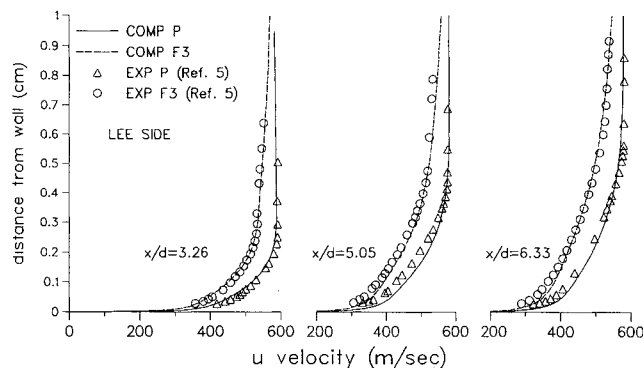

Fig. 13 Velocity profile comparisons, tips P and F3, $\alpha = 2.9$ deg, lee side.

worsen within about 0.05 cm from the wall, but with no clear trend. The comparisons of the R3 profiles relative to the P profiles show more favorable agreement. There is also close agreement with the recovery that the R3 profile exhibits over the three axial stations. On the wind side, both computation and experiment show the velocity deficit of the R3 profile relative to the P profile to be minimal. On the lee side, both show the boundary-layer edge of the spherical nosetip profiles to extend outward beyond the edge of the pointed nosetip profiles. There is also agreement in the outward migration of the merging of the profiles as x/d increases. The slight bulge in the measured wind side profiles at $x/d = 6.33$, 0.05 cm from the wall occurred for all nosetips.

Figures 12 and 13 show the velocity profile comparisons for nosetips P and F3, $\alpha = 2.9$ deg. Throughout most of the boundary layer, the absolute agreement between computation and experiment is within about 3%. As in the R3 nosetip case, the exception is at the second station on the lee side, where the agreement is only within about 8-9%. And again, the comparisons worsen within 0.05 cm from the wall, but with no clear trend. Both computation and experiment show the velocity deficit for the flat nosetip to be greater than for the spherical nosetip. Similar to the R3 profiles, the comparisons of the F3 profiles relative to the P profiles clearly show more favorable agreement than the absolute comparisons. There is also favorable agreement in the location where the P and F3 profiles merge. On the lee side, the effects of the flat nosetip on the profiles are most drastic; both computation and experiment show the lack of recovery of the F3 profile relative to the P profile.

Concluding Remarks

A thin-layer Navier-Stokes computational study has been made to simulate the effects of nosetip bluntness on a body of revolution at Mach 2.95. Two thin-layer Navier-Stokes codes that use an implicit Beam and Warming central-differencing algorithm were used to compute the viscous flow over the

model excluding the base region. Computational results were presented for pointed, spherical, and flat nosetip configurations.

Most of the comparisons of bow shock location, recompression shock location, and surface-pressure distribution were within the measurement accuracy. One exception was at the severe expansion at the abrupt corner of the flat nosetip, where the expansion was slightly smeared. Another exception was in the lee side flow region of the flat nosetip case, where the pressure was slightly underpredicted at one pressure tap just downstream of the corner. The flat nosetip computations did, however, show flow separation to exist downstream of the corner of the flat nosetip, a flow detail that is difficult, if not impossible, to detect from the shadowgraphs. The computational results provide evidence that a skewed grid that wraps around the corner of the flat nosetip is a viable approach for modeling the flowfield.

The comparisons of turbulent velocity profiles on the cylinder agreed to within 5% except close to the wall, where the agreement was slightly worse. It was determined that the velocity profiles were sensitive to boundary-layer transition, and so the computations were performed using the same transition intermittency distribution for all cases. In this regard, the effects of bluntness on the velocity profiles were found to be consistent between computation and experiment relative to the pointed nosetip case.

The computations presented here demonstrate a capability to predict some important flow details of pointed, spherical, and flat tipped (nonspinning) shell to a high degree of accuracy. Within the limitations of boundary-layer transition as encountered in this study, the computations serve as a benchmark for future CFD efforts in the modeling of supersonic flow over both spinning and nonspinning bodies of revolution. The accurate prediction of bluntness effects on Magnus characteristics of shell is an immediate goal in this research effort. Lastly, it is noted that one of the ongoing challenges is to reduce the computational intensiveness of the problem while ensuring that the accuracy of the flow details is not compromised.

References

[1]Sturek, W. B., Mylin, D. C., Guidos, B. J., and Nietubicz, C. J., "Navier-Stokes Computational Study of the Influence of Shell Geometry on the Magnus Effect at Supersonic Speeds," U.S. Army Ballistic Research Laboratory/ARRADCOM, ARBRL-TR-02501, Aberdeen Proving Ground, MD, June 1983.

[2]Kayser, L. D., "Effects of Small Nose Bluntness on Static Stability and Magnus Characteristics of a Projectile Shape at Mach 0.91 and 3.03," U.S. Army Ballistic Research Laboratory/AMC, BLR-MR-3535, Aberdeen Proving Ground, MD, July 1986.

[3]Dolling, D. S., and Bogdonoff, S. M., "Supersonic, High Reynolds Number Flow over a Tangent Ogive Cylinder at Small Angles of Attack: An Experimental Study and Comparison with Theory," Mechanical and Aerospace Engineering Dept., Princeton Univ., Rept. 1421-MAE, Princeton, NJ, Jan. 1979.

[4]Gray, W. K., Dolling, D. S., and Bogdonoff, S. M., "An Experimental Investigation of Tip Bluntness Effects on the Turbulent Compressible Boundary Layer on an Axisymmetric Body," Mechanical and Aerospace Engineering Dept., Princeton Univ., Rept. 1530-MAE, Princeton, NJ, May 1981.

[5]Dolling, D. S., and Gray, W. K., "Compilation of Wall Pressure and Turbulent Boundary Layer Data for Supersonic, High Reynolds Number Flow over a Blunted Tangent Ogive Cylinder at Small Angles of Attack," Mechanical and Aerospace Engineering Dept., Princeton Univ., Rept. 1585-MAE, Princeton, NJ, Sept. 1982.

[6]Dolling, D. S., and Gray, W. K., "Experimental Study of Supersonic Turbulent Flow on a Blunted Axisymmetric Body," AIAA Journal, Vol. 24, No. 5, 1986, pp. 793-799.

[7]Pulliam, T. H., and Steger, J. L., "Implicit Finite-Difference Simulations of Three-Dimensional Compressible Flow," AIAA Journal, Vol. 18, No. 2, 1980, pp. 159-167.

[8]Beam, R., and Warming, R. F., "An Implicit Factored Scheme for the Compressible Navier-Stokes Equations," AIAA Paper 78-0257, Jan. 1978.

[9]Rizk, Y. M., and Chaussee, D. S., "Three-Dimensional Viscous-Flow Computations Using a Directionally Hybrid Implicit-Explicit

Procedure," AIAA Paper 83-1910, July 1983.

[10]Kutler, P., Pedelty, J. A., and Pulliam, T. H., "Supersonic Flow over Three-Dimensional Ablated Nosetips Using an Unsteady Implicit Numerical Procedure," AIAA Paper 80-0063, Jan. 1980.

[11]Rizk, Y. M., Chaussee, D. S., and McRae, D. S., "Numerical Simulation of Viscous-Inviscid Interactions in Indented Nose Tips," AIAA Paper 82-0290, Jan. 1982.

[12]Pulliam, T. H., and Steger, J. L., "Recent Improvements in Efficiency, Accuracy, and Convergence for Implicit Approximate Factorization Algorithms," AIAA Paper 85-0360, Jan. 1985.

[13]Schiff, L. B., and Steger, J. L., "Numerical Simulation of Steady Supersonic Viscous Flow," AIAA Journal, Vol. 18, No. 12, 1980, pp. 1421-1430.

[14]Rai, M. M., and Chaussee, D. S., "New Implicit Boundary Procedures: Theory and Applications," AIAA Paper 83-0123, Jan. 1983.

[15]Schiff, L. B., and Sturek, W. B., "Numerical Simulation of Steady Supersonic Flow over an Ogive Cylinder Boattail Body," U.S. Army Ballistic Research Laboratory, ARBRL-TR-02363, Aberdeen Proving Ground, MD, Sept. 1981.

[16]Weinacht, P., Guidos, B. J., Kayser, L. D., and Sturek, W. B., "PNS Computations for Spinning and Fin-Stabilized Projectiles at Supersonic Speeds," U.S. Army Ballistic Research Laboratory, ARBRL-MR-3464, Aberdeen Proving Ground, MD, Sept. 1985.

[17]Baldwin, B. S., and Lomax, H., "Thin-Layer Approximation and Algebraic Model for Separated Turbulent Flows," AIAA Paper 78-0257, Jan. 1978.

[18]Dhawan, S., and Narasimha, R., "Some Properties of Boundary Layer Flow During the Transition from Laminar to Turbulent Motion," Journal of Fluid Mechanics, Vol. 3, 1958, pp. 418-436.

[19]Guidos, B. J., Weinacht, P., and Dolling, D. S., "Comparison of Navier-Stokes Computation and Experiment for Pointed, Spherical, and Flat Tipped Shell at Mach 2.95," AIAA Paper 90-0587, Jan. 1990.

[20]Buning, P. G., private communication, NASA Ames Research Center, Moffett Field, CA, 1986.

James E. Daywitt
Associate Editor